

Effects of Hydrothermal Temperature on Morphology and Electrochemical Performance of LiMnPO₄ Cathodes

Zhi Gao^{1,*}, Xiaoliang Pan^{1,*}, Yingying Zeng^{1,*}, Xiang Xia¹, Huiling Yuan¹, Yi Pei², Haihui Chen³

¹ School of Mechanical Engineering, Jingtangshan University, Jian 343009, China

² School of Materials Science and Engineering, Harbin Institute of Technology, Harbin 150001, China

³ School of Chemistry and Chemical Engineering, Jingtangshan University, Jian 343009, China

*E-mail: zhigaomail@gmail.com, xiaoliangpanmail@gmail.com

Received: 26 September 2015 / Accepted: 12 October 2015 / Published: 4 November 2015

Various morphologies of LiMnPO₄ crystals have been achieved controllably via a facile hydrothermal process. Effects of hydrothermal temperature on structure, morphology and electrochemical performance of LiMnPO₄ crystals have been systematically investigated by X-ray diffraction (XRD), scanning electron microscope (SEM) and charge/discharge measurement, respectively. A possible formation mechanism for these LiMnPO₄ crystals has been phenomenologically presented. The experimental results reveal that the hydrothermal temperatures have strong influences on the morphologies of the LiMnPO₄ crystals, and thus the subsequent electrochemical performances of the LiMnPO₄ cathodes. The prisms obtained at 200 °C exhibit the most homogeneous morphology, the greatest dispersibility, the least average crystal size, and deliver the highest discharge capacity of 145 mA h g⁻¹ at 0.05 C.

Keywords: LiMnPO₄ cathodes; hydrothermal temperature; electrochemical performance

1. INTRODUCTION

Lithium-ion batteries have been widely applied in many fields because of their excellent performance [1]. Cathodes are a key part of lithium-ion batteries [2]. Among candidates to replace the high cost and toxic cobalt based cathodes for lithium-ion batteries, LiMPO₄ ($M = \text{Mn, Fe and Ni}$) with ordered olivine structure are promising alternative cathode materials due to their low price, environmental friendliness, excellent cycling stability and superior safety performance [3-5]. In this olivine structure family, LiFePO₄ has been intensively investigated and commercially produced [6-8]. However, LiFePO₄ is known to have a low energy density owing to its lower voltage window (3.5 V vs. Li/Li⁺) [9]. LiMnPO₄ is an appealing alternative to LiFePO₄ [10], because it provides a higher

operating voltage (4.1 V vs. Li/Li⁺), and a ~20% higher gravimetric energy density [11]. Thereby, its use as cathode material is greatly expected [12]. Additionally, LiMnPO₄ is compatible with the present electrolytes [13], whereas LiCoPO₄ (4.8 V vs. Li/Li⁺) and LiNiPO₄ (5.1 V vs. Li/Li⁺) are not easily compatible with these electrolytes [14]. Nevertheless, LiMnPO₄ has much lower intrinsic electronic and ionic conductivities caused by the Jahn-Teller anisotropic lattice distortion in Mn³⁺ sites and the large volume change between LiMnPO₄ phase and MnPO₄ phase, resulting in poor electrochemical activities in lithium ion batteries [15-17]. Therefore, tremendous efforts have been made to overcome these problems for enhancing their electrochemical performances, including coating with fine electronic conductive materials, doping with alien ions, particle size reductions, and so on [18-20].

Recently, studies on LiMnPO₄ cathodes have clearly indicated that morphology plays a significant role in improvement in their electrochemical performances [21]. Correspondingly, many morphology-selective synthetic techniques have been developed to prepare high-performance LiMnPO₄ cathodes, including solvothermal method [22], sol-gel process [23], solid-state reaction [24], polyol technique [25], precipitation method [26], spray pyrolysis process [27], off-stoichiometry process [28], supercritical ethanol method [29], etc. Among these routes, the wet-chemical methods have been regarded as effective approaches to tune LiMnPO₄ morphology by properly controlling external experimental conditions such as temperature, pH value and concentration. For examples, by varying the pH value of the reaction suspension, the nanorods, the thick nanoplates (about 50nm in thickness) and the thin nanoplates (20-30 nm in thickness) were prepared via a solvothermal method, and the thin nanoplates displayed the best charge/discharge performance which was mainly ascribed to its excellent morphological advantages [30]. By manipulating the various experimental parameters such as the reactant feeding order, the reaction time, the pH value, the LiMnPO₄ nanomaterial was synthesized by a solvothermal approach, which presented a discharge capacity of 147 mA h g⁻¹ at 0.05 C [31]. By controlling the precursor concentration, the reaction time and the addition of the organic molecules, the different morphologies of the products could be obtained and the results of the charge/discharge measurements showed that the reversible capacity could be obviously improved by tailoring the morphology [32]. By appropriate adjustment of the pH value of the reactant and the precursor concentration, the prisms and the plates with hexagonal basal faces as well as the cuboids and the rod-like particles were produced via a microwave-assisted hydrothermal synthesis [33]. By tuning the synthesis parameters such as the concentration of the surfactants, the reaction temperature and time, the spherical, thin or thick nanorods, and the needle-shaped particles of the LiMnPO₄ cathodes were obtained via a thermal decomposition method, and the nanocomposite LiMnPO₄ electrode provided a discharge capacity of 165 mA h g⁻¹ at 1/40 C [34].

Although the above results exhibit improved electrochemical properties of the LiMnPO₄ cathodes by optimizing their external synthetic conditions, these syntheses involve complex procedures and/or costly reagents. Here, we report a facile hydrothermal method for controllable synthesis of LiMnPO₄ crystals with various morphologies by simply manipulating hydrothermal temperature in an organic-free system. A possible formation mechanism of the resulting LiMnPO₄ samples is proposed. The relationship between the morphology and the electrochemical performance of the LiMnPO₄ cathodes is elucidated.

2. EXPERIMENTAL

2.1 Materials synthesis

All the reagents were commercially available and used as received. 20 mmol $\text{Na}_2\text{S}\cdot 9\text{H}_2\text{O}$, 40 mmol $\text{Li}_2\text{SO}_4\cdot \text{H}_2\text{O}$, 40 mmol $\text{MnSO}_4\cdot \text{H}_2\text{O}$, 40 mmol $\text{NH}_4\text{H}_2\text{PO}_4$ were used as starting materials, and added in sequence in a 40 mL Teflon liner with 30 mL distilled water under constant stirring condition for 30 min. The obtained suspensions were transferred into Teflon-lined stainless steel autoclaves, sealed and heated for 10 h in electric ovens at different temperatures from 120 °C to 200 °C to get the products.

2.2 Materials Characterization

The X-ray diffraction (XRD, Rigaku D/max-rA diffractometer, Cu $K\alpha$ radiation, $\lambda = 1.5406 \text{ \AA}$) was used to characterize phase of sample. The field-emission scanning electron microscope (FE-SEM, FEI Quanta 200F) was employed to observe morphology of sample.

The as-prepared LiMnPO_4 sample was mixed with 20 wt. % of Super P by the ball milling at 200 rpm for 1 h in a 50 mL stainless steel vial using five around 5 mm diameter stainless steel balls. Then, the mixture was annealed at 700 °C for 10 h in an Ar atmosphere to obtain the LiMnPO_4/C composites. To fabricate the cathode, 87.5 wt. % LiMnPO_4/C composites, 2.5 wt. % Super P and 10 wt. % polyvinylidene fluoride (PVDF) were thoroughly mixed together, making the final active material (LiMnPO_4), carbon and binder in weight ratio of 70:20:10. Subsequently, the mixture was uniformly pasted onto an aluminium foil using a scraper, and dried in an oven at 60 °C. After drying, the foil was punched into circular discs, pressed with pressure, dried in vacuum at 120 °C for 10 h, and then assembled into 2032 coin-type cells in an argon-filled glovebox (Mbraun, Unilab, Germany). Pure lithium foil was used as the counter electrode. The electrolyte consisted of a solution of 1 M LiPF_6 in ethylene carbonate and dimethyl carbonate (EC + DMC, 1:1 in volume).

The electrochemical measurements were performed using the 2032 coin-type cells with a Land-CT2001A battery test system (Jinnuo Wuhan Corp., China). The cells were charged at galvanostatic mode to 4.5 V, held at 4.5 V until 0.05 C, and then discharged at galvanostatic mode to 2.4 V. The electrochemical impedance spectroscopy (EIS) measurements of the cells were carried out on a CHI 660E electrochemical workstation (Chenhua Instruments Shanghai Inc., China). An ac voltage signal of 5 mV was used in frequency range of 0.01 to 100,000 Hz. All the electrochemical measurements were carried out at room temperature.

3. RESULTS AND DISCUSSION

3.1 Phase impurity and crystal structure

Figure 1 shows the XRD patterns of the as-prepared LiMnPO_4 samples synthesized for 10 h at the different temperatures from 120 °C to 200 °C. The JCPDS card pattern of LiMnPO_4 is also shown

for comparison (rod pattern at the bottom of figure). The diffraction peaks of the samples obtained at the hydrothermal temperatures from 140 °C to 200 °C are identified as those of LiMnPO_4 with an orthorhombic olivine-type structure. However, the impurity peaks are detected when the hydrothermal reaction is conducted at a temperature of 120 °C (Figure 1e). The results indicate that a high temperature is essential for the formation of pure LiMnPO_4 crystals. On the other hand, it is suggested that Teflon loses its strength and stainless steel exposed to caustic mixtures undergoes caustic embrittlement at temperatures above 200 °C, which can quickly ruin an autoclave. For preventing this potential risk, the highest hydrothermal temperature of 200 °C is selected in our work.

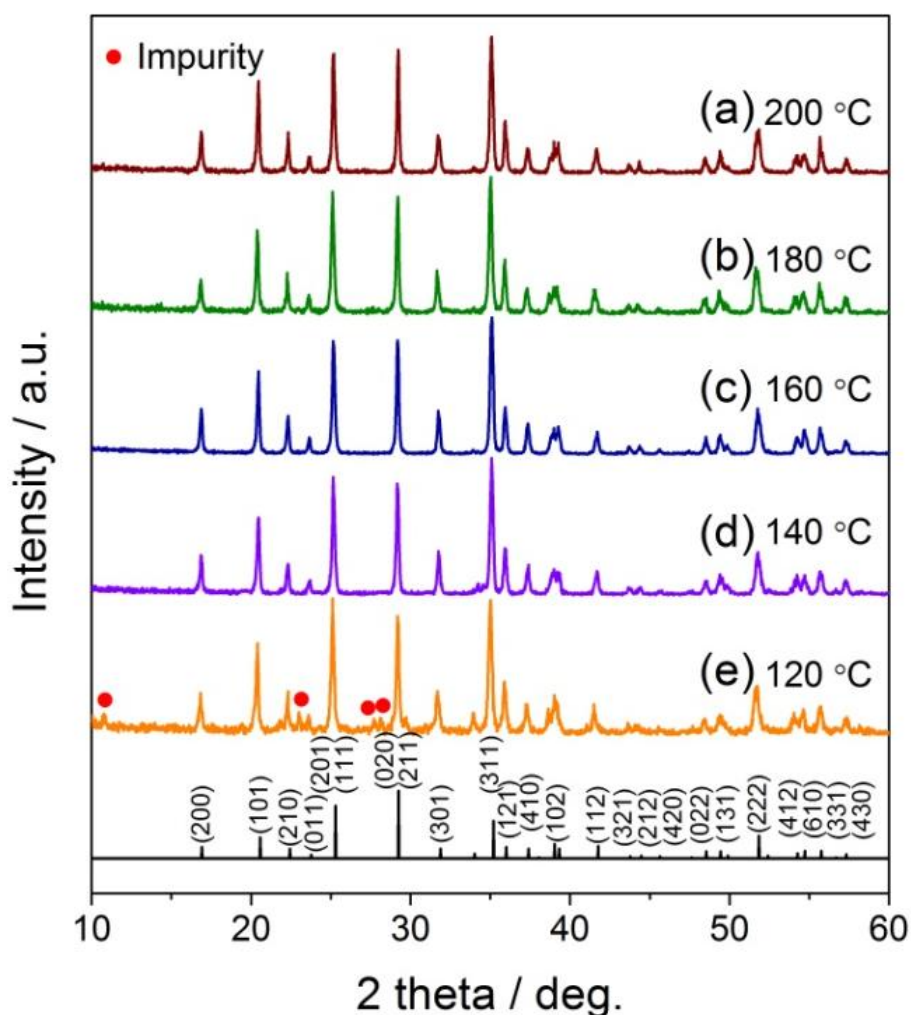


Figure 1. XRD patterns of the as-prepared LiMnPO_4 samples synthesized for 10 h at different temperatures from 120 °C to 200 °C.

As shown in Figure 2a and 2b, the LiMnPO_4 sample obtained at 140 °C displays a dumbbell-like morphology. The dumbbells with lengths of ~ 60 μm and diameters of ~ 20 μm are hierarchically constructed with the tiny prisms, while these prisms are attached side by side in an ordered fashion. When the hydrothermal temperature gradually increases to 160 °C, the LiMnPO_4 microspheres are obtained (Figure 2c and 2d). The microspheres with diameters of 15 - 30 μm comprise the prism-like

crystals with a mean diameter of ca. 500 nm and length of about 4.5 μm which attach together through the ends and assemble into microspheres.

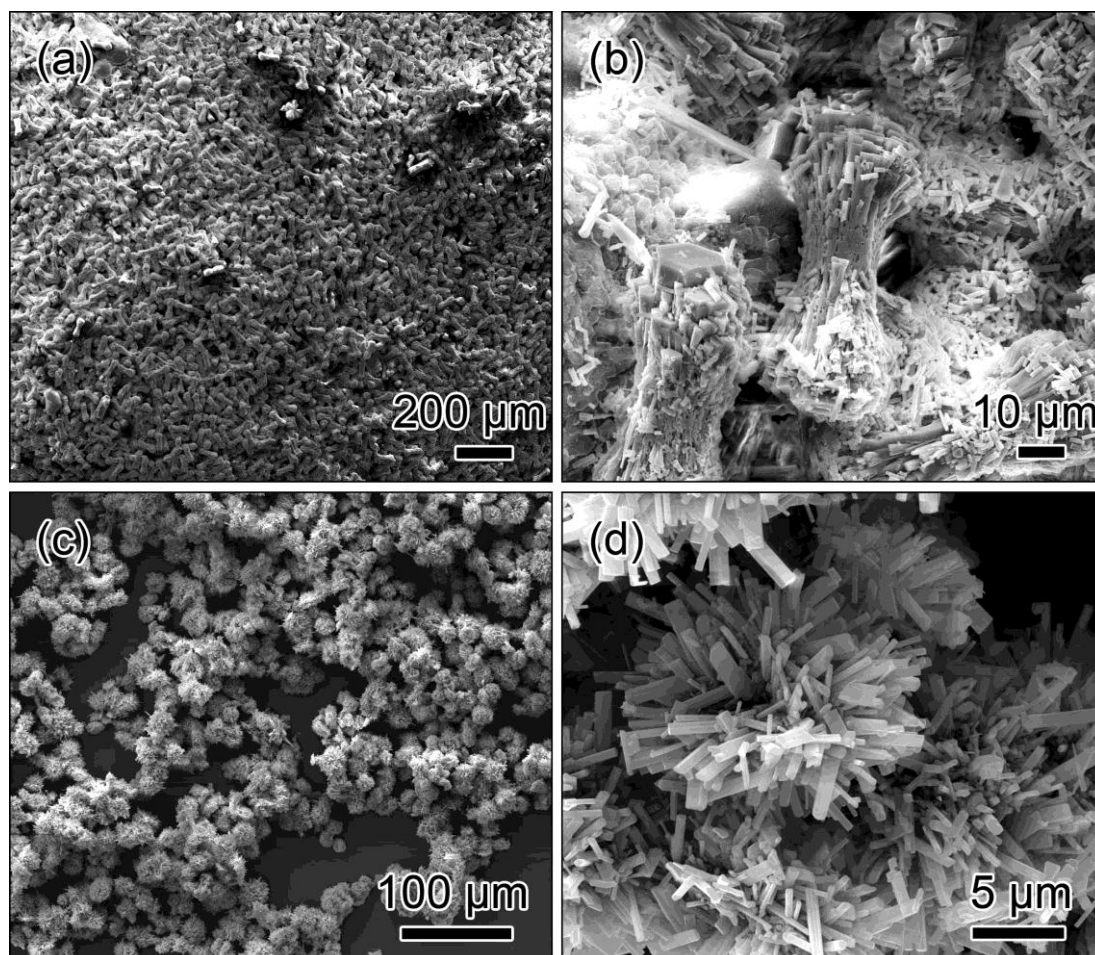


Figure 2. SEM images of the dumbbells (a and b) and the microspheres (c and d) prepared at 140 $^{\circ}\text{C}$ and 160 $^{\circ}\text{C}$, respectively.

As the hydrothermal temperature further increases to 180 $^{\circ}\text{C}$ (Figure 3a and 3b), the morphology of the LiMnPO_4 sample changes into the dispersed and nonuniform prisms (denoted as the coarse prisms in comparison to the prism prepared at 200 $^{\circ}\text{C}$). The coarse prisms have an average length of ca. 10 μm . While the hydrothermal temperature is up to 200 $^{\circ}\text{C}$, the LiMnPO_4 sample is consisted of the dispersed and uniform prisms (Figure 3c and 3d). The prisms with around 1 μm length and about 100 nm thickness have homogenous particle sizes and uniform shapes.

It can be seen from the above results that the hydrothermal temperature can strongly affect the morphology and the size of the LiMnPO_4 sample. Besides, the LiMnPO_4 sample obtained at the hydrothermal temperature of 200 $^{\circ}\text{C}$ has the least particle size and a well uniform morphology.

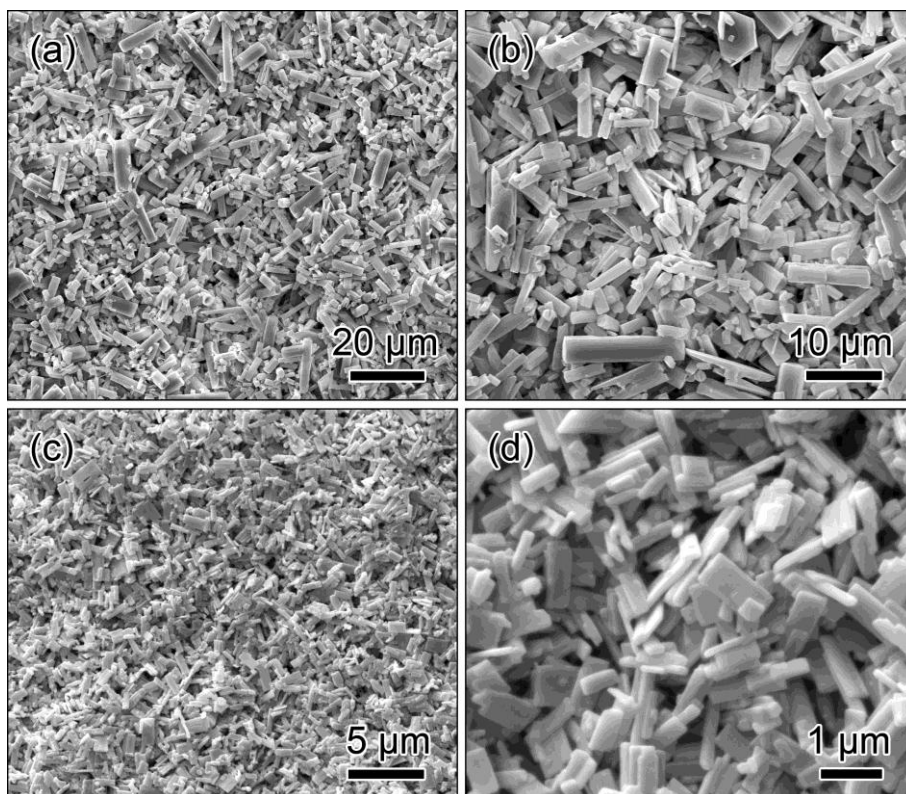


Figure 3. SEM images of the coarse prisms (a and b) and the prisms (c and d) prepared at 180 °C and 200 °C, respectively.

3.2 Formation mechanism analysis

According to our previous related work [35], $\text{Na}_2\text{S}\cdot 9\text{H}_2\text{O}$ was employed as an alkaline reagent to adjust the pH value of the solution in synthesis, since an alkaline condition was necessary for precipitating LiMnPO_4 samples in a hydrothermal synthesis. Meanwhile, the splitting process was proposed to elucidate the growth mechanism of the LiMnPO_4 crystals prepared with $\text{Na}_2\text{S}\cdot 9\text{H}_2\text{O}$. Generally, crystal splitting depends strongly on the reaction temperature associated with different degrees of splitting [36,37]. Hence, the effects of the hydrothermal temperatures on the morphologies of the samples are carefully investigated as described above.

With a lower reaction temperature of 140 °C, the morphology of the as-obtained products is mainly the dumbbells. With the temperature increases to 160 °C, the microspheres are obtained. When the temperature is above 180 °C, the LiMnPO_4 samples have a dispersed morphology. To understand the phenomenon of the changes in morphologies of the LiMnPO_4 crystals, we look into the relationships of the hydrothermal temperature and the splitting rate as well as the degree.

In the initial stage of the reaction, the splitting blocks are rapidly formed. Due to the fast growth caused by the great supersaturation, the distance of the growth front for the splitting blocks decreases significantly. The narrow boundary layer leads to instabilities that ultimately promote branching [37]. Then, the tiny prism-like splitting crystals are readily formed at the two heads of the splitting blocks. As the reaction proceeds, the tiny prisms bundles are produced via the continuous

crystal splitting.

At low hydrothermal temperature (140 °C), the splitting rate and the degree of the crystals are not high. The tiny prisms bundles can not split from the two heads of the splitting blocks. Finally, the dumbbell-like morphology is directly obtained (shown in Figure 2a and 2b).

As the hydrothermal temperature increases to 160 °C, the splitting rate and the degree of the prisms bundles at the two heads of the splitting blocks are increased. Meanwhile, it should be noted that the freshly-formed tiny prisms always deviate from the orientation of the splitting blocks, which can result in the formation of the 3D microsphere-like morphology via the repeated and successive multistep-splitting growth (shown in Figure 2c and 2d).

When the hydrothermal temperature increases further, the growth speed of the freshly-formed tiny prisms can not afford a connection between the neighbored splitting crystals under the effect of splitting mechanism, causing that the prism-like crystals are split from the splitting blocks, and the formation of the dispersed morphology. Moreover, because a greater splitting degree and a shorter growth period on the splitting blocks associated with a faster splitting rate, the crystal sizes and the shapes of the prisms obtained at 200 °C (shown in Figure 3c and 3d) are more uniform than that of the coarse prisms prepared at 180 °C (shown in Figure 3a and 3b).

In brief, the LiMnPO_4 crystals synthesized at the different temperatures in the hydrothermal processes can take on the different degrees of the splitting, resulting in a number of the subforms of the split crystals. On the basis of the above discussion, the strategy to control the morphology of the LiMnPO_4 crystals is summarized in Figure 4.

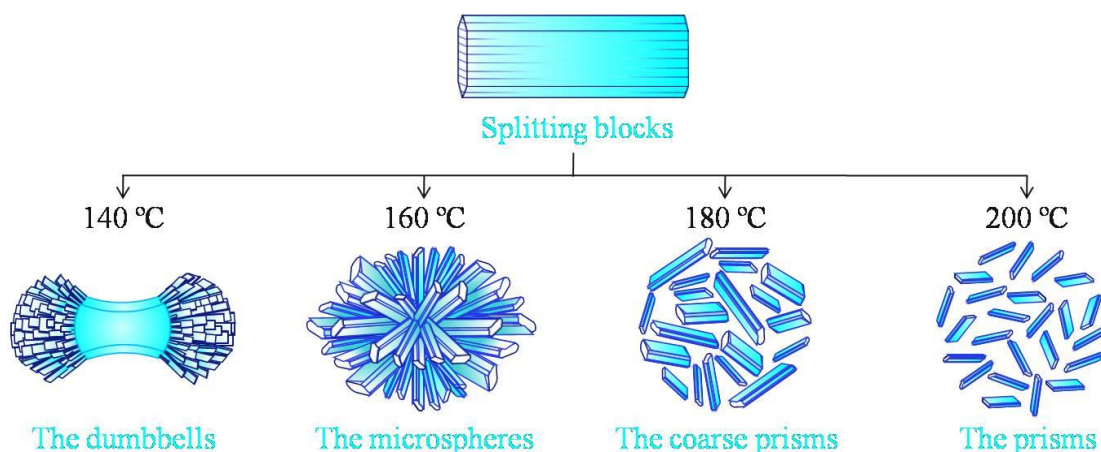


Figure 4. Schematic illustration of the variation of the morphologies for the LiMnPO_4 samples with the effects of the hydrothermal temperatures.

3.3 Electrochemical properties measurements

The electrochemical performances of the LiMnPO_4 crystals with different morphologies are understood by the charge/discharge tests, which are carried out from 0.05 C to 1 C between 2.4 and 4.5 V vs. Li/Li^+ at 25 °C. The typical results are shown in Figure 5. The discharge curves of all the LiMnPO_4 crystals at 0.05 C clearly show a long flat potential plateau at around 4.1 V (vs. Li/Li^+),

indicating that the two-phase redox reaction proceed between LiMnPO_4 and MnPO_4 in pure olivine-structured cathodes. The discharge capacity of the prisms is 145 mA h g^{-1} , and specially, the discharge plateau extends constantly up to about 100 mA h g^{-1} (Figure 5d), whereas the coarse prisms (Figure 5c), the microspheres (Figure 5b) and the dumbbells (Figure 5a) exhibit only 120, 110 and 76 mA h g^{-1} , respectively. It can be found that the prisms deliver a larger discharge capacity than other morphological samples. This difference can also be observed as the LiMnPO_4 crystals are discharged at higher rates. In detail, the prisms discharge 133 mA h g^{-1} at 0.1 C, 124 mA h g^{-1} at 0.2 C, 115 mA h g^{-1} at 0.5 C, and 108 mA h g^{-1} at 1 C. The coarse prisms exhibit discharge capacities of 105, 91, 78, and 69 mA h g^{-1} at 0.1 C, 0.2 C, 0.5 C and 1 C, respectively. The microspheres discharge 92 mA h g^{-1} at 0.1 C, 80 mA h g^{-1} at 0.2 C, 69 mA h g^{-1} at 0.5 C, and 60 mA h g^{-1} at 1 C. The discharge capacities of the dumbbells are 59, 51, 45, and 39 mA h g^{-1} at 0.1 C, 0.2 C, 0.5 C and 1 C, respectively.

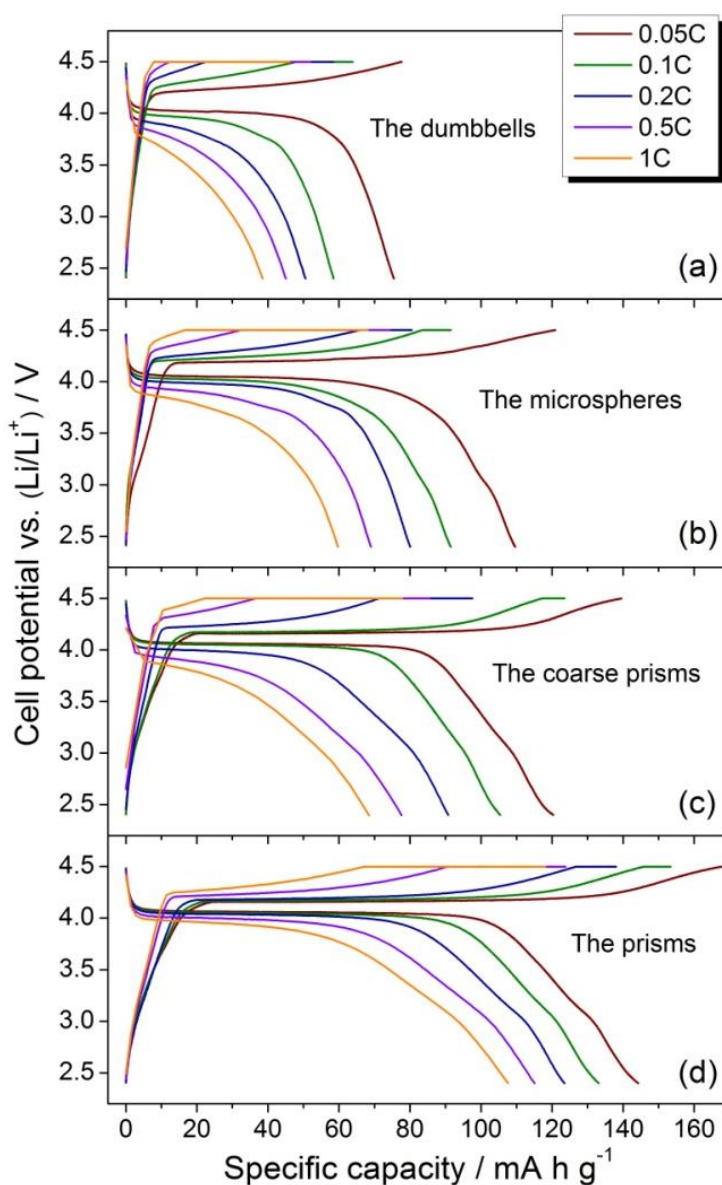


Figure 5. The charge/discharge curves of the LiMnPO_4 crystals with different morphologies.

Apparently, for all the LiMnPO_4 crystals the flat potential plateaus shorten and the discharge capacities decrease with increasing the rates. Diffusion polarization at higher rates brings this outcome [38]. It means that lithium ion motion is slower for the distribution to reach equilibrium than other steps in the electrochemical reaction such as the rate of the charge transfer. In addition, the prisms in our work exhibit comparable discharge capacities to some of the best reported LiMnPO_4 samples prepared via other synthesis methods in recent literatures [27, 31, 39-42].

From the above charge/discharge results, it can be safely concluded that the resulting LiMnPO_4 crystals exhibit the considerable morphology-dependent discharge capacities, which clearly demonstrate that the hydrothermal temperature is an important factor for the discharge performance improvement. When the low hydrothermal temperatures are applied, the poor dispersibility and the coarse grain for the LiMnPO_4 crystals may be simultaneously obtained, and thus leading to the decreased electrochemical performances, although the lower hydrothermal temperatures facilitate the experimental manipulation. As the hydrothermal temperature is up to 200 °C, the prisms can be readily obtained, which clearly present higher discharge capacity and better rate capability than those of the samples synthesized at lower temperatures. The SEM images indicate that the prisms have good dispersion morphology as well as fine crystal size, leading to increase in surface contact area between cathode and electrolyte, and to reduction in Li^+ diffusion length in crystal. Correspondingly, the large surface contact area is beneficial to reduction in the contact impedance, and the short Li^+ diffusion length is helpful for reduction in the diffusion resistance, resulting in fast interfacial charge transfer and high Li^+ diffusion flux [17]. Finally, the prisms exhibit much improved electrochemical performances.

To further confirm the stability as cathodes in lithium ion batteries, the cyclic performances of the LiMnPO_4 crystals with different morphologies are determined at 0.1 C in cell potential range of 2.4-4.5 V. The obtained result is shown in Figure 6. The discharge capacities keep almost unchanged after 50 cycles, showing that all the LiMnPO_4 crystals have a good cycling stability. The discharge capacity loss during the cycles can be ascribed to some origins such as the manganese dissolution, the electrolyte decomposition and the structure volume change [27,43,44]. After a total 50 cycles, the discharge capacity of 124 mA h g^{-1} is still achieved for the prisms, and 93% of the initial discharge capacity is retained. The coarse prisms, the microspheres and the dumbbells display the capacities of 97, 85 and 55 mA h g^{-1} at the 50th cycle against the initial discharge capacities of 105, 92 and 59 mA h g^{-1} , respectively.

To understand the effects of the LiMnPO_4 morphologies on the electrochemical performance of the cells described above, EIS measurements of all the cells at the fully discharged state are carried out at room temperature. Both working (LiMnPO_4) and counter (lithium) electrode have a diameter of 16.0 mm. It should be pointed out, that a geometrical asymmetry is not intended, but an axial shift between working and counter electrode of 0-0.5 mm is inevitable and non-reproducible among our experiments. Prior to the EIS measurements, all the cells are discharged to 2.4 voltage after completing 50th cycle at 0.1 C and maintained at the open circuit voltage for 10 h.

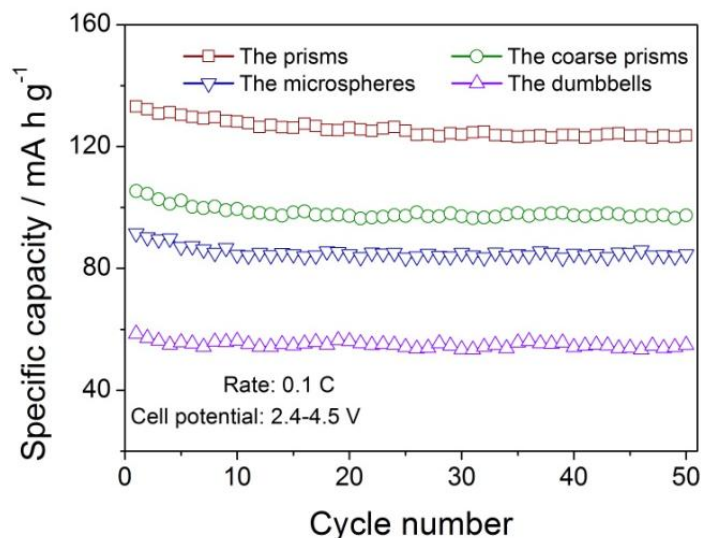


Figure 6. The cycling performance curves of the LiMnPO_4 crystals with different morphologies at a rate of 0.1 C in cell potential range of 2.4-4.5 V.

The results of the measurements are shown in Figure 7. As shown on the figure, all the spectra are similarly composed of one semicircle at the high frequency region and a sloping line at the low frequency range. It can be clearly observed that the size of the semicircle is strongly dependent on the LiMnPO_4 morphology. A smaller semicircle is obtained from the cell of the prisms, indicating that the impedance value of the prisms is lower than that of the others. It can be attributed to the decreasing of lithium ion migration and/or charge transfer resistance in the LiMnPO_4 electrode with the prisms, which may be explained by the larger surface area and greater dispersibility as well as smaller crystal size for the prisms allowing better exposure of active materials to the electrolyte. These results are in good agreement with the SEM images observation and the charge/discharge test.

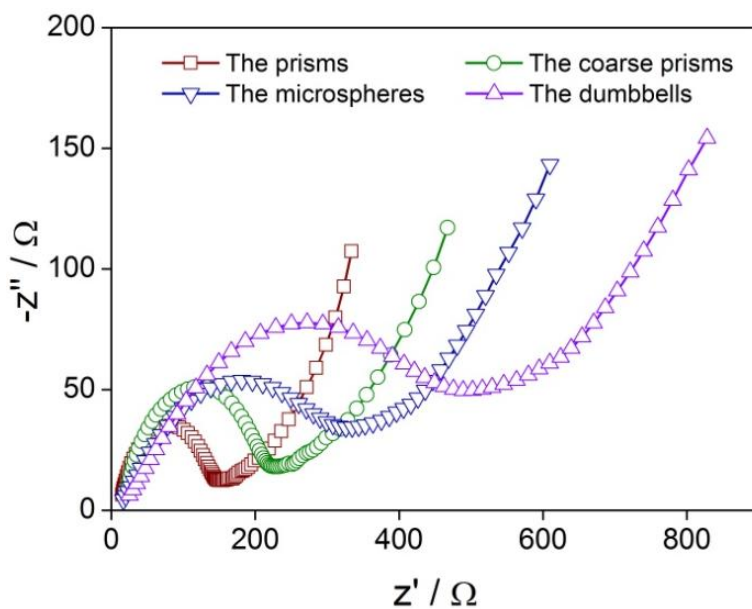


Figure 7. Impedance spectra of LiMnPO_4 electrodes with various morphologies.

4. CONCLUSIONS

In summary, we have successfully synthesized various morphologies of LiMnPO₄ crystals by a facile hydrothermal method, and have clearly demonstrated that the hydrothermal temperature has an important impact on the morphology of the LiMnPO₄ crystals, and affects the electrochemical performance of the LiMnPO₄ cathodes. At low hydrothermal temperatures, the dumbbells, the microspheres and the coarse prisms may be prepared. At 200 °C, the prisms can be obtained, which exhibit the most homogeneous morphology, the greatest dispersibility, the least average crystal size and the best electrochemical performances in terms of discharge capacity, rate capability and cycling stability among all the hydrothermally synthesized LiMnPO₄ crystals. The prisms give a discharge capacity of 145 at 0.05 C and a capacity retention of 93% at 0.1 C after 50 cycles. These improved properties are ascribed to its morphology advantages.

ACKNOWLEDGEMENTS

This work is supported by the National Natural Science Foundation of China (51564024) and the Major Science & Technology Program of Jiangxi Province (20143ACB21024) and the Science & Technology Supporting Program of Jiangxi Province (20133BBE50010 and 20122BBE500047) and the Science & Technology Transformation Program of Jiangxi Provincial Education Department (KJLD12080) and the Science & Technology Supporting Program of Jian City (JA2014-36-09) and the Doctoral Starting up Foundation of Jinggangshan University (JZB15005).

References

1. M. Armand, and J. M. Tarascon, *Nature*, 451 (2008) 652.
2. M. S. Whittingham, *Chem. Rev.*, 104 (2004) 4271.
3. A. K. Padhi, and K. S. Nanjundaswamy, J. B. Goodenough, *J. Electrochem. Soc.*, 144 (1997) 1188.
4. J. Kim, K. Y. Park, I. Park, J. K. Yoo, D. H. Seo, S. W. Kim, and K. Kang, *J. Electrochem. Soc.*, 159 (2012) A55.
5. R. V. Hagen, H. Lorrman, K. C. Möller, and S. Mathur, *Adv. Energy Mater.*, 2 (2012) 553.
6. A. Yamada, S. C. Chung, and K. Hinokuma, *J. Electrochem. Soc.*, 148 (2001) A224.
7. F. Zhou, P. Zhu, X. Fu, R. Chen, R. Sun, and C. P. Wong, *CrystEngComm*, 16 (2014) 766.
8. W. T. Geng, and T. Ohno, *J. Phys. Chem. C*, 117 (2012) 276.
9. N. S. Norberg, and R. Kostecki, *J. Electrochem. Soc.*, 159 (2012) A1431.
10. G. H. Li, H. Azuma, and M. Tohda, *Electrochem. Solid-State Lett.*, 6 (2002) A135.
11. D. Chen, W. Wei, R. Wang, X. F. Lang, Y. Tian, and L. Guo, *Dalton Trans.*, 41 (2012) 8822.
12. V. Aravindan, J. Gnanaraj, Y. S. Lee, and S. Madhavi, *J. Mater. Chem. A*, 1 (2013) 3518.
13. D. Choi, D. Wang, I. T. Bae, J. Xiao, Z. Nie, W. Wang, V. V. Viswanathan, Y. J. Lee, J. G. Zhang, G. L. Graff, Z. Yang, and J. Liu, *Nano Lett.*, 10 (2010) 2799.
14. S. M. Oh, S. T. Myung, Y. S. Choi, K. H. Oh, and Y. K. Sun, *J. Mater. Chem.*, 21 (2011) 19368.
15. S. P. Ong, V. L. Chevrier, and G. Ceder, *Phys. Rev. B*, 83 (2011) 075112.
16. Y. K. Sun, S. M. Oh, H. K. Park, and B. Scrosati, *Adv. Mater.*, 23 (2011) 5050.
17. K. Dokko, T. Hachida, and M. Watanabe, *J. Electrochem. Soc.*, 158 (2011) A1275.
18. L. E. Li, J. Liu, L. Chen, H. Xu, J. Yang, and Y. Qian, *RSC Adv.*, 3 (2013) 6847.
19. V. Ramar, and P. Balaya, *Phys. Chem. Chem. Phys.*, 15 (2013) 17240.
20. J. Yoshida, M. Stark, J. Holzbock, N. Hüsing, S. Nakanishi, H. Iba, H. Abe, and M. Naito, *J. Power Sources*, 226 (2013) 122.

21. N. P. W. Pieczonka, Z. Liu, A. Huq, and J. H. Kim, *J. Power Sources*, 230 (2013) 122.
22. P. Nie, L. Shen, F. Zhang, L. Chen, H. Deng, and X. Zhang, *CrystEngComm*, 14 (2012) 4284.
23. J. Zong, and X. Liu, *Electrochim. Acta*, 116 (2014) 9.
24. L. Zhang, Q. Qu, L. Zhang, J. Li, and H. Zheng, *J. Mater. Chem. A*, 2 (2014) 711.
25. D. Wang, H. Buqa, M. Crouzet, G. Deghenghi, T. Drezen, I. Exnar, N. H. Kwon, J. H. Miners, L. Poletto, and M. Grätzel, *J. Power Sources*, 189 (2009) 624.
26. K. Su, F. Liu, and J. Chen, *J. Power Sources*, 232 (2013) 234.
27. T. N. L. Doan, and I. Taniguchi, *J. Power Sources*, 196 (2011) 1399.
28. B. Kang, and G. Ceder, *J. Electrochem. Soc.*, 157 (2010) A808.
29. D. Rangappa, K. Sone, Y. Zhou, T. Kudo, and I. Honma, *J. Mater. Chem.*, 21 (2011) 15813.
30. Z. Qin, X. Zhou, Y. Xia, C. Tang, and Z. Liu, *J. Mater. Chem.*, 22 (2012) 21144.
31. S. L. Yang, R. G. Ma, M. J. Hu, L. J. Xi, Z. G. Lu, and C. Y. Chung, *J. Mater. Chem.*, 22 (2012) 25402.
32. H. Ji, G. Yang, H. Ni, S. Roy, J. Pinto, and X. Jiang, *Electrochim. Acta*, 56 (2011) 3093.
33. C. Neef, C. Jähne, H. P. Meyer, and R. Klingeler, *Langmuir*, 29 (2013) 8054.
34. N. H. Kwon, and K. M. Fromm, *Electrochim. Acta*, 69 (2012) 38.
35. X. L. Pan, C. Y. Xu, and L. Zhen, *CrystEngComm*, 14 (2012) 6412.
36. J. Tang, and A. P. Alivisatos, *Nano Lett.*, 6 (2006) 2701.
37. A. G. Kanaras, C. Sönnichsen, H. Liu, and A. P. Alivisatos, *Nano Lett.*, 5 (2005) 2164.
38. S. Wang, H. Yang, L. Feng, S. Sun, J. Guo, Y. Yang, and H. Wei, *J. Power Sources*, 233 (2013) 43.
39. J. K. Kim, C. R. Shin, J. H. Ahn, A. Matic, and P. Jacobsson, *Electrochem. Commun.*, 13 (2011) 1105.
40. Z. Yang, G. S. Cao, J. Xie, and X. B. Zhao, *J. Solid State Electrochem.*, 3 (2012) 1271.
41. J. Liu, X. Liu, T. Huang, and A. Yu, *J. Power Sources*, 229 (2013) 203.
42. J. Zong, and X. Liu, *Electrochim. Acta*, 116 (2014) 9.
43. Q. Y. Hao, S. A. Liu, X. M. Yin, Z. F. Du, M. Zhang, L. M. Li, Y. G. Wang, T. H. Wang, and Q. H. Li, *CrystEngComm*, 13 (2011) 806.
44. M. Pivko, M. Bele, E. Tchernychova, N. Z. Logar, R. Dominko, and M. Gaberscek, *Chem. Mater.*, 24 (2012) 1041.